Nano Research
2022, 15(10): 8819–8825

ISSN 1998-0124 CN 11-5974/O4
https://doi.org/10.1007/s12274-022-4565-2

Research Article

Pd-Sn alloy nanoparticles for electrocatalytic methanol oxidation: Phase evolution from solid solution to intermetallic compounds

Jinna Xue[1], Zheng Hu[1] (✉), Hui Li[1,2], Yu Zhang[1,2], Chang Liu[1], Min Li[1], Qiuhua Yang[1] (✉), and Shi Hu[1,2] (✉)

[1] *Department of Chemistry, School of Science, Tianjin Key Laboratory of Molecular Optoelectronic Science, Tianjin University, Tianjin 300072, China*
[2] *Institute of Energy, Hefei Comprehensive National Science Center, Hefei 230000, China*

© Tsinghua University Press 2022

Received: 1 April 2022 / **Revised:** 12 May 2022 / **Accepted:** 20 May 2022

ABSTRACT

Developing efficient catalysts with high activity and durability via alloying strategy is essential to the energy conversion in various electro-catalytic reactions. Among the different alloy structures, intermetallic compounds (IMCs) have received much attention recently due to the special geometric and electronic effects and outstanding activity and durability, endowed by their ordered structure. Herein, A series of hollow-structured nanocrystals of Pd-Sn alloy, including face-centered cubic solid solution of Pd(Sn), IMCs of Pd_2Sn, and IMCs of Pd_3Sn_2, are fabricated via a solvothermal strategy by varying the precursor ratio of Pd and Sn. The structure difference of the nanocrystals has been investigated via combined electron microscopy and spectroscopy, assisted by local elemental separation analysis and X-ray spectroscopy. Among all, Pd_3Sn_2 IMCs show outstanding methanol oxidation reaction (MOR) activity in terms of mass activity (1.3 $A \cdot mg_{Pd}^{-1}$) and specific activity (5.03 $mA \cdot cm^{-2}$). Through density functional theory (DFT) simulation calculations on three different Pd-Sn alloy models, the performance has been well understood. As compared with Pd(Sn) and Pd_2Sn, the high MOR kinetics on Pd_3Sn_2 is featured by its weaker CO adsorption and favorable CO–OH co-adsorption.

KEYWORDS

Pd-Sn alloy, intermetallic compound, hollow structure, electrocatalysis, methanol oxidation reaction

1 Introduction

Noble metal-based nanomaterials have attracted much attention in the past decades for their irreplaceable role in catalyzing many important reactions [1–3]. The catalytic performance is driven by the reaction kinetics, which can be determined by the activation energy of the reaction and described by the adsorption energy of the intermediates [4, 5]. Meanwhile, the adsorption energy is in turn dependent on the electronic structure of the catalyst, which is correlated with its physical structure and especially the surface structure [6]. While Pt-group metals have long been demonstrated as superior electrocatalysts for processes likes hydrogen evolution reaction (HER), oxygen reduction reaction (ORR), and methanol oxidation reaction (MOR) [7–9], the limited activity and low abundance still call for new synthetic innovation in their alloys with precise control, enhanced activity, higher durability, and insightful understanding of mechanism [10–12].

The structure of binary alloys usually falls into three categories, including heterostructure, solid solution, and intermetallic compound (IMC) [13–15]. The choice of structure is thermodynamically determined by the interaction between the like and unlike atoms, but experimentally dependent on the synthetic protocols and requires great expertise [16–18]. Among them, IMC has been proven to be an effective candidate to form highly active and durable alloy catalysts, as it is driven by the favorable interaction between the unlike atoms [14, 19]. Huang's group reported the synthesis of ultrathin nanowires (NWs) of A1-phase palladium-copper alloy, which was transformed into an intermetallic B2 phase (PdCu-B2 NWs) by electrochemical treatment at room temperature [20]. For the reduction reaction (HER), the PdCu nanostructures with the intermetallic B2 phase show enhanced electrocatalytic activity in both acidic and basic media as compared to the A1 phase. The density functional theory (DFT) calculation results indicate that the B2 phase nanostructure has more "suitable" hydrogen binding energies and lower water dissociation activation energies than the disordered counterparts. Jeong et al. prepared disordered Pt_3Co alloy nanowires (D-Pt_3Co NWs) and fully ordered Pt_3Co intermetallic nanowires (O-Pt_3Co NWs) catalysts by confined nano-spatial orientation using mesoporous silica templates [21]. O-Pt_3Co NWs exhibit superior oxygen reduction activity and stability over D-Pt_3Co NWs and Pt/C. Combining DFT calculation results and experimental evidence, it is found that the excellent intrinsic catalytic activity of ordered intermetallic compounds can be attributed to the enhanced ligand effect in the subsurface. Importantly, the membrane electrode assembly (MEA) test indicates the excellent durability of O-Pt_3Co NWs in proton exchange membrane fuel cell (PEMFC) single-cell.

The Pd-Sn system has received special attention as Sn forms a large library of IMCs and solid solution with palladium, providing plenty of room for the study of structure–control and structure–performance relationship. The incorporation of Sn not only reduces the use of the expensive Pd but also improves the electronic structure of the noble metal [22–25]. In addition, the oxygen affinity of Sn effectively removes the intermediate

Address correspondence to Zheng Hu, inabahu@tju.edu.cn; Qiuhua Yang, qiuhuay@tju.edu.cn; Shi Hu, rychushi@gmail.com

adsorbed on the surface and reduces the Pd poisoning, thereby improving the catalytic activity and durability [26–28]. In the study of Du and co-workers, a series of grid-like PdSn nanomaterials prepared by the modified polyol method were employed as efficient anode catalysts for direct alcohol fuel cells [29]. The X-ray photoelectron spectroscopy (XPS) results clearly indicated that the introduction of Sn changed the electronic structure of Pd, which played an important role in improving the MOR activity. Huang et al. synthesized wavy Pd_4Sn nanowires, which exhibited high activity and stability in ORR and MOR [30]. The improvement of MOR activity and stability comes from the vacancy structure (especially the Sn vacancy structure) caused by surface defects, which reduces the activation energy of the MOR process and increases the energy barrier of the CO poisoning process. While various alloys of Pd-Sn have been studied as promising electrocatalysts for MOR, there is still huge room for improvement.

Herein, a series of Pd-Sn alloy nanoparticles (NP) with hollow structure were obtained via a solvothermal method. The alloy structure evolves from Pd-Sn solid solution to Pd_3Sn_2 and Pd_2Sn IMCs with the increase of Sn/Pd ratio. The catalytic evaluation manifests that the hollow Pd_3Sn_2 IMC possesses the best electrocatalytic activity and durability for MOR in alkaline medium, as compared with the other two catalysts, i.e., Pd_2Sn and Pd(Sn) solid solution. The proper spatial distribution of Pd and Sn in Pd_3Sn_2 has led to suitable electronic structure and favorable co-adsorption of CO and OH, which weakened the adsorption of CO and contribute to the excellent performance.

2 Experimental

2.1 Materials and chemicals

All the reagents were of analytical grade and used without further purification. Palladium(II) acetylacetonate ($Pd(acac)_2$) was purchased from Aldrich Chemistry; tin(II) chloride dihydrate ($SnCl_2{\cdot}2H_2O$) was purchased from Sinopharm Chemical Reagent Co., Ltd. (Shanghai, China); polyvinylpyrrolidone (PVP, K 29-32) was purchased from Macklin; N,N-dimethylformamide (DMF) was purchased from Tianjin Yuanli Chemical industry Co., Ltd. (Tianjin, China). Vulcan XC-72R carbon was supplied by Cabot Corp. Potassium hydroxide (KOH, 95%) was purchased from Meryer. Methanol solution was purchased from Shanghai Aladdin Biochemical Technology. Nafion (5 wt.%) was purchased from Sigma-Aldrich. Ar (99.999%) was purchased from Tianjin Yekong High-Tech Gas Co., Ltd.

2.2 Synthesis of Pd_xSn_y NP catalysts

The Pd_xSn_y alloy nanoparticles were prepared by reference to the synthesis of excavated cubic platinum-tin alloy [31]. Pd_3Sn_2 was synthesized with a precursor Sn/Pd ratio of 1:1. In a hydrothermal synthesis reactor, 12 mL of DMF was added, followed by 0.02 mmol of $Pd(acac)_2$, 0.02 mmol of $SnCl_2{\cdot}2H_2O$, and 0.3 g of PVP. After stirring and dissolving, the autoclave was transferred into a 200 °C oven and reacted for 6 h. The resulting solution was centrifuged and washed with deionized water, and then dried in vacuum. Pd(Sn), Pd_2Sn, and Sn(Pd) were synthesized by similar methods with Sn/Pd ratio of 1:4 (0.008 mmol of $SnCl_2{\cdot}2H_2O$ and 0.032 mmol of $Pd(acac)_2$), 2:3 (0.016 mmol of $SnCl_2{\cdot}2H_2O$ and 0.024 mmol of $Pd(acac)_2$), and 4:1 (0.032 mmol of $SnCl_2{\cdot}2H_2O$ and 0.008 mmol of $Pd(acac)_2$), respectively, with all the other conditions unchanged. The synthesis of pure Pd (or Sn) was to remove the precursor of Sn (or Pd) under the same other conditions.

2.3 Materials characterization

Transmission electron microscopy (TEM, JEOL-1230) was used to characterize the morphology of the products. High-resolution TEM (HRTEM), high-angle annular dark field scanning TEM (HAADF-STEM), and energy dispersive X-ray spectroscopy (EDS) mapping were performed on a JEOL JEM-F200 transmission electron microscope. The crystal structure of the sample was analyzed by X-ray diffractometry (XRD) at room temperature using a D8-Focus diffractometer (Bruker AXS) with a Cu Kα radiation source (40 kV, 40 mA, and λ = 1.5418 Å). The XPS was performed using an ESCALAB-250Xi spectrometer (Thermo Fisher Scientific) with Al Kα X-ray. The amount of three Pd-Sn samples for the electro-catalytic reaction was determined by inductively coupled plasma optical emission spectrometry (ICP-OES, Agilent 720).

2.4 Electrochemical measurements

The electrochemical analysis was performed on a CHI-660 potentiostat (CH Instruments, Austin, TX, USA). A typical three-electrode system was used in the measurement, with a glassy-carbon (GC, diameter of 4 mm) electrode as the working electrode, a platinum foil as the counter electrode, and a Hg/HgO electrode as the reference electrode. For electrochemical test, the carbon black powder (Vulcan XC-72R, Cabot) was used as the support for all the as-obtained alloy nanoparticles. The loading of metals in the carbon-supported catalyst was 20%: 2 mg of the alloy and 8 mg of the carbon were dispersed in 1 mL of isopropanol and mixed with 990 μL of pure water. Then 10 μL of Nafion (5.0 wt.%) was added before ultrasonication for 1 h to form a uniformly dispersed suspension. The ink was cast onto the GC electrode to form an even film, with a metal loading of 40 $\mu g{\cdot}cm^{-2}$.

For electrochemical test, cyclic voltammetry (CV) was performed in argon-saturated 1.0 M KOH and 1.0 M KOH added with 1.0 M methanol solution respectively, at a sweep rate of 50 $mV{\cdot}s^{-1}$. The electrochemically active surface area (ECSA) of the catalysts was calculated by integrating the oxidation charge of CO stripping on the CV in the 1.0 M KOH solution. For CO stripping test, first, CO was bubbled into 1.0 M KOH for 20 min, followed by another 10 min with the potential held at 0.08 V. Argon gas was then introduced for 30 min to remove the excess CO. Finally, CO was stripped by scanning CV from 0.05 to 1.2 V at a sweep rate of 10 $mV{\cdot}s^{-1}$.

3 Results and discussion

In the presence of $Pd(acac)_2$, $SnCl_2{\cdot}2H_2O$, PVP, and DMF, Pd-Sn nanoparticles with different compositions were obtained through a solvothermal method at 200 °C for 6 h. Three types of hollow Pd-Sn nanocrystals were obtained by tuning the ratio of $SnCl_2{\cdot}2H_2O$ and $Pd(acac)_2$ at 1:4, 2:3, and 1:1. The actual atomic ratio of Sn to Pd was determined by the EDS and ICP-OES (Fig. S1 and Table S1 in the Electronic Supplementary Material (ESM)). The results obtained by the two analytical methods are similar and very close to the theoretical feed ratio.

As shown in the XRD pattern (Fig. S2 in the ESM), the products obtained with a molar ratio of Sn/Pd = 1/4 (blue line) retain a typical face-centered cubic (fcc) structure, just as pristine Pd. The diffraction angle shifts to a lower end to that of Pd (JCPDS: 46-1043) as the doping of larger Sn (metallic radius: 140 pm) expands the crystal lattice of Pd (131 pm) [22]. A clear hollow structure can be identified from the TEM and HRTEM images (Figs. 1(a) and 1(b)), which could be attributed to the Kirkendall effect [32–34]. It is reasonable as Pd is more easily reduced from its precursor as compared to Sn. Hence, Pd nanoparticles will be generated in the reaction and act as the

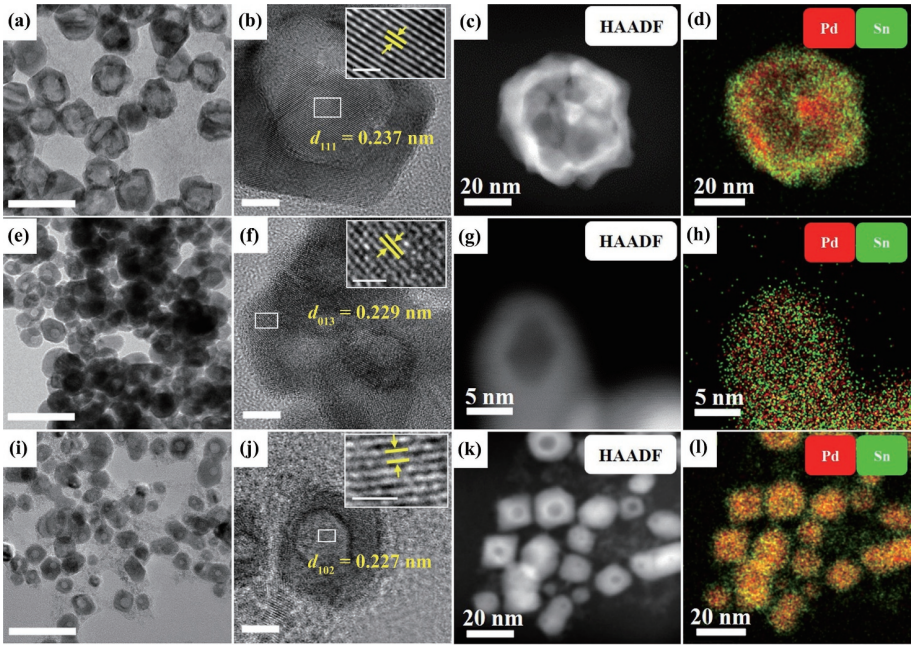

Figure 1 (a) TEM image, (b) HRTEM image (inset: enlarged view of local area), (c) HAADF image, and (d) EDS mapping of nanoparticles with Sn/Pd molar ratio of 1:4. TEM, HRTEM, HAADF, and EDS images of Sn to Pd of 2:3 ((e)–(h)) and 1:1 ((i)–(l)), respectively. The scale bars in TEM ((a), (e), and (i)) and HRTEM ((b), (f), and (j)) images are 50 and 5 nm, respectively. The scale bars in the insets of (b), (f), and (j) are 1 nm.

template for the hollow structure, with Pd out-diffusing against the inward-diffusing Sn. In comparison, the TEM image of the product obtained with only Pd precursor shows solid nanoparticles (Fig. S3 in the ESM), while the XRD diffraction peaks show clear shift to the lower angle (black line in Fig. S2 in the ESM), due to the formation of palladium hydride. The peak size in the TEM-based histogram of the hollow nanoparticles is around 25 nm (Fig. S4(a) in the ESM). The HRTEM image (Fig. 1(b)) confirms the crystalline feature of the hollow structure, which shows a lattice spacing of 0.237 nm, slightly larger than that of fcc Pd (111) (0.225 nm) and consistent with the XRD shift. The EDS mapping of the product confirms the mixing of the two elements although slight enrichment of Sn at the surface can be identified (Fig. 1(d)). It supports the above hypothesis that the Sn was grown on the preformed Pd nanoparticles and the structure underwent incomplete mixing.

When more Sn is introduced into the host, the alloy structure underwent further transformation into an ordered one. As shown in the XRD pattern (green line in Fig. S2 in the ESM) of the products obtained from Sn/Pd = 2/3, an IMC phase of Pd_2Sn (JCPDS: 52-1515) can be identified. The particle size is smaller (12 nm, Fig. S4(b) in the ESM) but the hollow feature is retained (Figs. 1(e)–1(g)). The lattice spacing in Fig. 1(f) (0.229 nm) can be attributed to the {013} crystal plane of Pd_2Sn IMC while the mixing of Pd and Sn is more uniform with less element enrichment.

When the Sn/Pd ratio increases to 1, the XRD pattern (red line in Fig. S2 in the ESM) can be indexed to Pd_3Sn_2 IMC (JCPDS: 04-0801). The peak size sampled from the TEM images is around 13 nm (Fig. S4(c) in the ESM). The lattice fringes in Fig. 1(j) (0.227 nm) are consistent with the interplanar spacing of {102} planes in the hexagonal Pd_3Sn_2. A darker ring can be identified in the center part of the hollow structure. It is clearer in the high-contrast region of the HAADF-STEM image (Fig. 1(k)). The central part should be attributed to the unalloyed Pd, which has a density (12.0 $g{\cdot}cm^{-2}$) much higher than that of Pd_3Sn_2 (10.2 $g{\cdot}cm^{-2}$). The EDS elemental mapping clearly indicates the near-uniform mixing of Pd and Sn in the nanoparticles, with some residue Sn left between the nanoparticles (Fig. 1(l)). It makes up for the difference between the stoichiometry of the crystalline phase and the ICP-EDS results. The Pd and Sn distribution is further investigated by the local element separation (LES) method developed by us recently. The heatmap of the LES matrix was derived from the EDS mapping signal of Pd and Sn (Figs. 2(a) and 2(b)). As shown in Fig. 2(c), the yellow regions indicate a Pd/Sn ratio higher than average (Pd-rich) and the blue regions lower than average (Sn-rich). The bright yellow pixels in the heatmap match well with the high-brightness part in the HAADF-STEM image, confirming the enrichment of Pd in the center of the nanoparticles. The residual Sn around the alloy nanoparticles could be easily identified in the navy regions of the heatmap.

While the series of hollow structured nanoparticles can be obtained with the element ratio as in the precursor, we will use Pd(Sn), Pd_2Sn, and Pd_3Sn_2 to indicate the samples with Sn/Pd feed ratio of 1:4, 2:3, and 1:1 for the following discussion, respectively. Although more IMC types can be identified from the phase diagram (Fig. S5 in the ESM), they were not obtained under the experimental conditions, as confirmed by the single Pd_3Sn_2 crystalline phase in the sample obtained with Sn/Pd ratio of 4 (Fig. S2 in the ESM).

The hollow structure is featured by large surface area, which is beneficial to catalysis by exposing more active sites. The MOR activity of the series of Pd-Sn catalysts was evaluated in alkaline media. As shown in the CV in a 1 M KOH electrolyte (Fig. S6 in the ESM), the hydrogen adsorption peak can be observed in the range of 0.05–0.4 V vs. reversible hydrogen electrode (RHE) while the peak between 0.4–1.2 V (vs. RHE) can be attributed to the hydroxyl adsorption/desorption. Pd_3Sn_2 exhibits lower OH desorption potential (0.722 V) than Pd_2Sn and Pd(Sn), corresponding to high OH binding energy (BE).

The electrochemical MOR for the Pd-Sn alloy catalysts was conducted by CV measurement in an Ar-saturated solution containing 1 M KOH and 1 M CH_3OH. Here, the current density was normalized by the ECSA calculated from CO stripping which is 25.8 $m^2{\cdot}g^{-1}$ for Pd_3Sn_2, 25.8 $m^2{\cdot}g^{-1}$ for Pd_2Sn, and 21.7 $m^2{\cdot}g^{-1}$ for Pd(Sn), as shown in Fig. 3(a) and Fig. S7 in the ESM. Pd_3Sn_2 has the lowest onset potential and the highest peak current density in term of specific activity (Fig. 3(b)). This could be explained by the most negative CO desorption potential of Pd_3Sn_2 as compared to the other samples (Fig. 3(a)). As shown in Fig. 3(c), Pd_3Sn_2 has

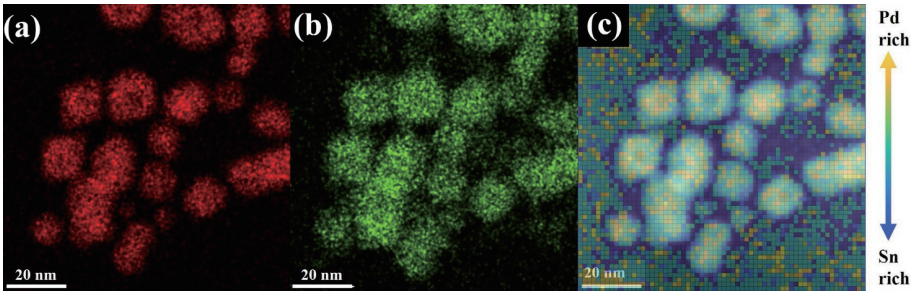

Figure 2 (a) and (b) EDS mapping of Pd and Sn in the alloy nanoparticles with Sn/Pd ratio of 1, and (c) the local elemental separation heatmap derived from the EDS mapping.

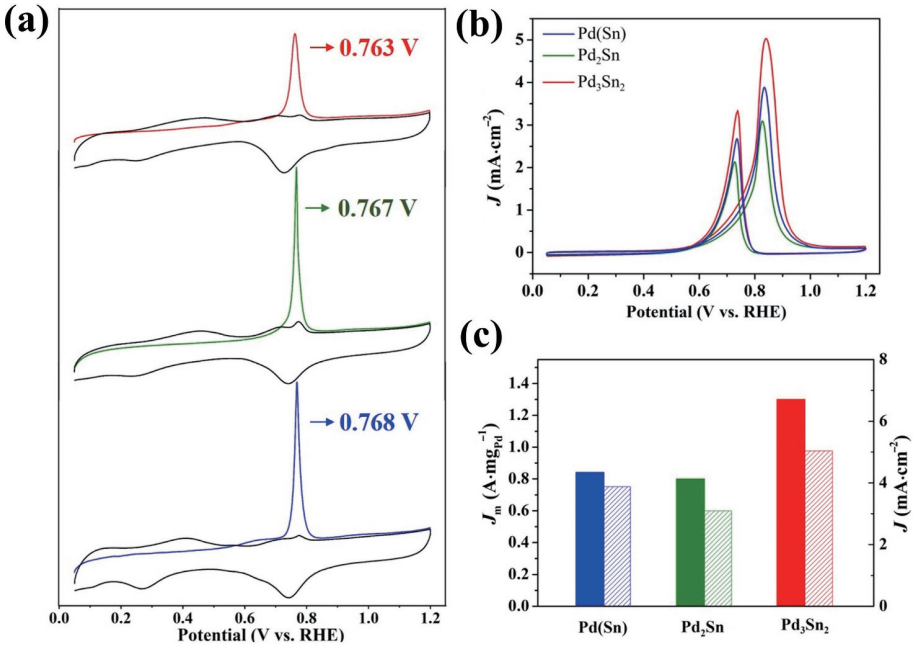

Figure 3 Electrochemical evaluation of Pd_3Sn_2, Pd_2Sn, and Pd(Sn). (a) CO stripping in Ar-saturated 1.0 M KOH at a scan rate of 10 mV·s^{-1}. (b) Methanol oxidation in aqueous solution containing 1.0 M KOH and 1.0 M methanol (scan rate: 50 mV·s^{-1}). (c) Comparison of the mass activities and specific activities of different catalysts towards methanol oxidation.

the highest mass activity (1.3 A·mg$_{Pd}^{-1}$) and specific activity (5.03 mA·cm^{-2}), which are 1.6 and 1.5 times those of Pd_2Sn, respectively. The superior performance of Pd_3Sn_2 was also consolidated via chronoamperometry. After holding the potential at 0.74 V (vs. RHE) for 7,200 s, the residual mass activity of Pd_3Sn_2 (50.3 A·g$_{Pd}^{-1}$) is 1.4 and 2.2 times those of the Pd_2Sn (36.3 A·g$_{Pd}^{-1}$) and fcc Pd(Sn) (23.3 A·g$_{Pd}^{-1}$), respectively, illustrating the excellent stability of Pd_3Sn_2 (Fig. S8 in the ESM). Therefore, the results demonstrate that the Pd_3Sn_2 phase exhibits superior MOR performance in both activity and durability.

To investigate the relationship between the structure and performance in these Pd-Sn alloy, XPS was used to probe the difference in their electron structure. In all the samples, the peak area for Sn in the oxidized state is clearly larger than that of Sn in the metallic state (Figs. 4(a)–4(c)). The calculated ratio of Sn^0 to $Sn^{2+/4+}$ is 29.2:70.8 in Pd(Sn), 21.6:78.4 in Pd_2Sn, and 24.2:75.8 in Pd_3Sn_2. It should be noted that Sn is easily oxidized and not all Sn is alloyed with Pd or forming Pd-Sn IMC. In this regard, the XPS of Pd is more informative than that of Sn. The Pd 3d spectra indicate that the majority of Pd in Pd(Sn), Pd_2Sn, and Pd_3Sn_2 is in metallic state, as is shown in Figs. 4(d)–4(f). Both the Pd $3d_{3/2}$ and $3d_{5/2}$ peaks of Pd_2Sn (Fig. 4(e)) can be fitted by three peaks, indicating the presence of Pd in three different oxidation states. The Pd $3d_{5/2}$ peaks typically have BE of 335.1, 335.7, and 336.2 eV. The peak at 336.2 eV is attributed to surface oxidation while the other two peaks are related to the two different Pd atoms in the crystal structure of Pd_2Sn and Pd_3Sn_2. The diminishment of peak at 335.1 eV in Pd_3Sn_2 is related to the reduced ratio of Pd species in the channels of the crystal structure (1/3 as compared to 1/2 in Pd_2Sn), as is shown in Fig. S9 in the ESM.

Further understanding of the activity difference in the Pd-Sn alloy can be consolidated by the DFT calculation. Based on the bifunctional mechanism [35], CO and OH adsorption energies are efficient descriptor for the MOR activity. To find the spatial distribution of CO and OH adsorption, the difference in CO and OH adsorption energy between different sites of the catalyst models was studied, including Pd_3Sn_2, Pd_2Sn, and Pd(Sn) with 25% Sn doping (simplified model for the Pd(Sn) solid solution). As shown in Fig. S10 in the ESM, the green and orange points were stable or meta-stable CO (green) and OH (orange) adsorption sites in the Pd-Sn alloy surface. CO tends to adsorb on the Pd sites and OH tends to adsorb on the Sn sites or Pd/Sn bridge sites. Hence, the synergetic effects of Pd and Sn exhibit as different adsorption preference in the CO and OH. Moreover, CO and OH tend to be distantly dispersed in Pd_2Sn and closely dispersed in Pd_3Sn_2 and Pd(Sn) models. Because the adsorbed CO molecules were lastly oxidized by the adjacent OH group, the spatial proximity of CO and OH was able to highly influence the kinetics of surface CO removal. To further understand the influence of CO and OH distribution, the most stable CO/OH co-adsorption configuration is shown in Fig. 5(a) and the C–O partial pair distribution function (PDF) of different models is plotted in

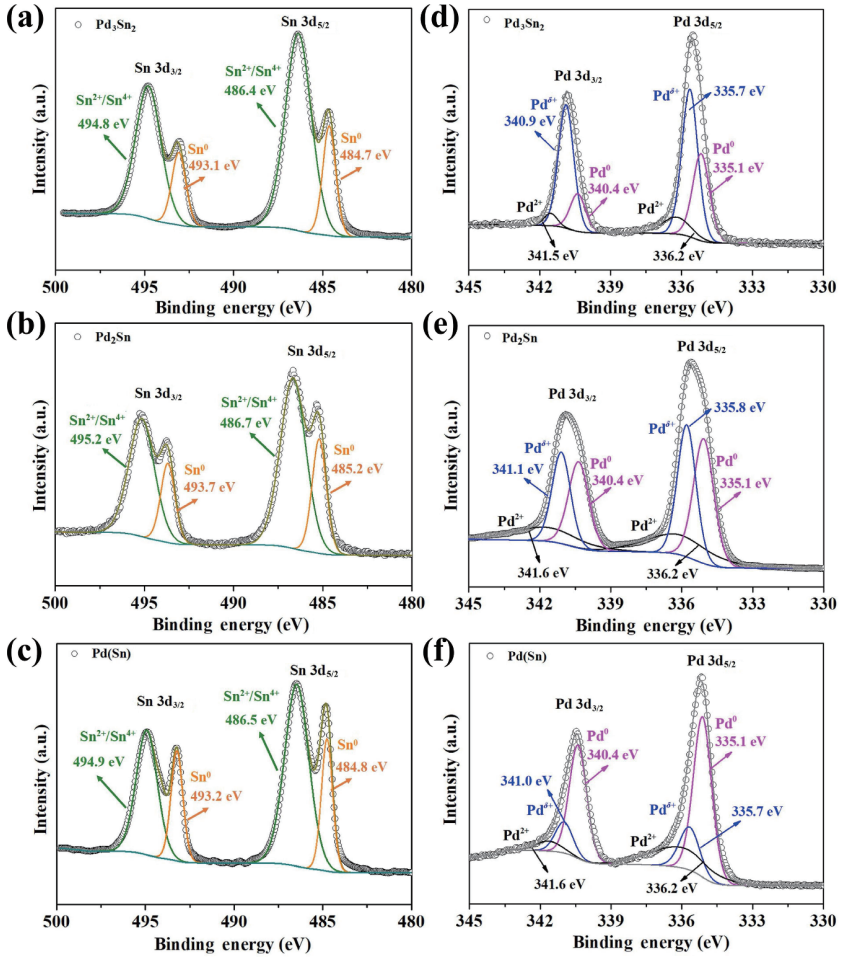

Figure 4 XPS of ((a)–(c)) Sn 3d and ((d)–(f)) Pd 3d for ((a) and (d)) Pd_3Sn_2, ((b) and (e)) Pd_2Sn, and ((c) and (f)) Pd(Sn). The Sn^{2+} and Sn^{4+} species are very close in BE to be differentiated.

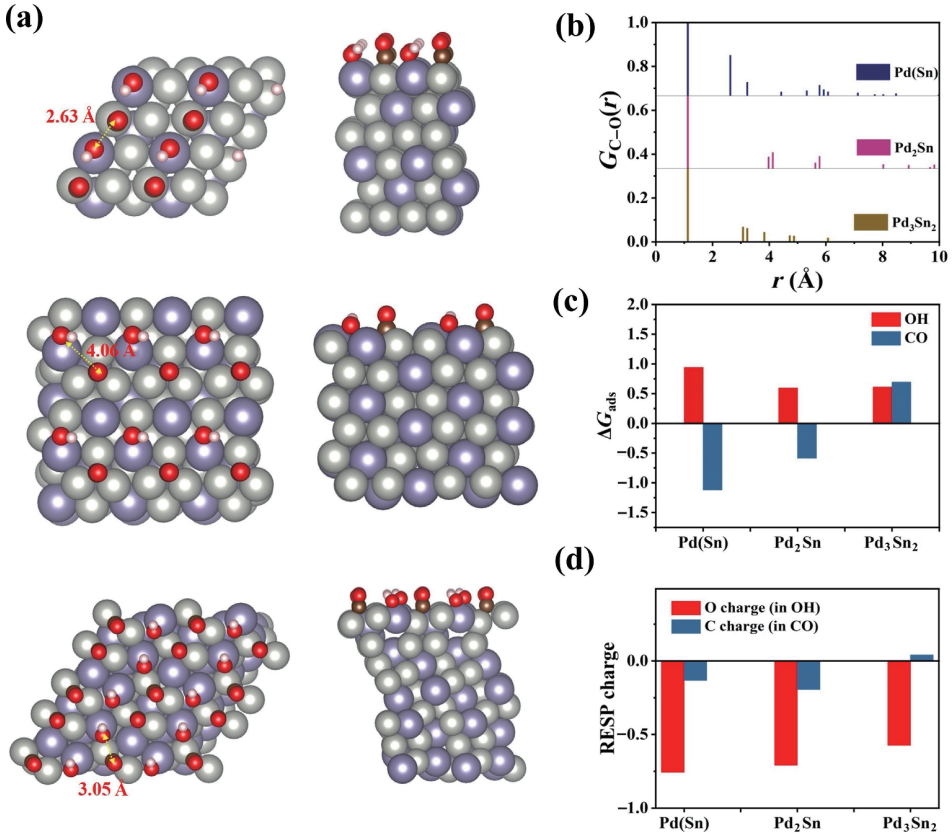

Figure 5 (a) The most stable CO and OH co-adsorption configuration on Pd-Sn alloy models including Pd(Sn) with 25% doping, Pd_2Sn, and Pd_3Sn_2. (b) C–O partial pair distribution function of the models. (c) Adsorption energy of CO and OH in the Pd(Sn), Pd_2Sn, and Pd_3Sn_2 models. (d) RESP charge of C (in CO molecule) and O (in OH group) adsorbed on the Pd(Sn), Pd_2Sn, and Pd_3Sn_2 surface.

Fig. 5(b). The distances of the second and third shells O in the catalyst models are 2.6 and 3.2 Å for Pd(Sn), 3.1 and 3.2 Å for Pd_3Sn_2, and 4.0 and 4.1 Å for Pd_2Sn. Among them, the Pd_2Sn model has the longest CO–OH distance while Pd(Sn) the shortest.

On the other hand, the adsorption energy was compared to distinguish the difference in adsorption energy among the catalyst models. As shown in Fig. 5(c), the CO adsorption shows big difference in different Pd-Sn models while the OH adsorption is almost unaffected. The CO adsorption energy in the Pd_3Sn_2 model is +0.69 eV, which indicates greater anti-poisoning characteristics. The Pd(Sn) model has the most negative CO adsorption energy and the most surface sites of Pd due to the low doping level. Hence, a large part of Pd(Sn) surface could be poisoned because the adsorbed OH cannot convert all the adjacent strongly-bonded CO molecules. The charge feature was also studied to unveil the interaction between CO and the substrate. The restrained electrostatic potential (RESP) charges of C (in CO molecule) and O (in OH group) were fitted (Fig. 5(d) and Fig. S10 in the ESM). The C atoms have more positive charge in the Pd_3Sn_2 model, which indicates less electron transfer from Pd, while the transfer in Pd(Sn) and Pd_2Sn models is more significant. To sum up, Pd_3Sn_2 is featured by weaker CO adsorption and favorable CO–OH co-adsorption, which contributes to its high MOR kinetics as compared with Pd(Sn) and Pd_2Sn.

4 Conclusions

To summarize, a facile approach has been developed to synthesize a novel class of binary Pd-Sn alloy nanoparticles with a hollow structure. The increased doping of Sn leads to the evolution from Pd-Sn solid solution to Pd-Sn IMCs of Pd_2Sn and Pd_3Sn_2. IMC of higher Sn/Pd ratio cannot be obtained with this method, even with excess Sn addition. The structure difference after Sn introduction effectively modifies the electronic structure of the alloy, which further regulates the absorption energy of the reaction intermediate. When the Sn/Pd feed ratio is 1/1, the resultant Pd_3Sn_2 IMC shows the highest catalytic MOR activity (1.3 $A{\cdot}mg_{Pd}^{-1}$ and 5.03 $mA{\cdot}cm^{-2}$) among all. Based on the DFT calculation results, the change in the electronic structure has led to weakened adsorption of CO and favorable co-adsorption of CO and OH, which contributes to the excellent performance of Pd_3Sn_2.

Acknowledgements

The authors acknowledge support from the Natural Science Foundation of Tianjin, China (No. 18JCYBJC20600) and Institute of Energy, Hefei Comprehensive National Science Center (No. 19KZS207).

Electronic Supplementary Material: Supplementary material (detailed supporting figures of TEM, XRD, XPS, electrocatalytic MOR measurement, and DFT calculation information) is available in the online version of this article at https://doi.org/10.1007/s12274-022-4565-2.

References

[1] Kua, J.; Goddard, W. A. Oxidation of methanol on 2nd and 3rd row group VIII transition metals (Pt, Ir, Os, Pd, Rh, and Ru): Application to direct methanol fuel cells. *J. Am. Chem. Soc.* **1999**, *121*, 10928–10941.

[2] Hui, F.; Li, C.; Chen, Y. H.; Wang, C. H.; Huang, J. P.; Li, A.; Li, W.; Zou, J.; Han, X. D. Understanding the structural evolution of $Au/WO_{2.7}$ compounds in hydrogen atmosphere by atomic scale *in situ* environmental TEM. *Nano Res.* **2020**, *13*, 3019–3024.

[3] Liu, C.; Chen, Z. L.; Rao, D. W.; Zhang, J. F.; Liu, Y. W.; Chen, Y. N.; Deng, Y. D.; Hu, W. B. Behavior of gold-enhanced electrocatalytic performance of NiPtAu hollow nanocrystals for alkaline methanol oxidation. *Sci. China Mater.* **2021**, *64*, 611–620.

[4] Xu, C. J.; Zhang, Y.; Chen, J.; Li, S.; Zhang, Y. W.; Qin, G. W. Carbon–CeO_2 interface confinement enhances the chemical stability of Pt nanocatalyst for catalytic oxidation reactions. *Sci. China Mater.* **2021**, *64*, 128–136.

[5] Lou, W. H.; Ali, A.; Shen, P. K. Recent development of Au arched Pt nanomaterials as promising electrocatalysts for methanol oxidation reaction. *Nano Res.* **2022**, *15*, 18–37.

[6] Zhan, C. Y.; Li, H. Q.; Li, X. M.; Jiang, Y. Q.; Xie, Z. X. Synthesis of $PdH_{0.43}$ nanocrystals with different surface structures and their catalytic activities towards formic acid electro-oxidation. *Sci. China Mater.* **2020**, *63*, 375–382.

[7] Chen, A. C.; Holt-Hindle, P. Platinum-based nanostructured materials: Synthesis, properties, and applications. *Chem. Rev.* **2010**, *110*, 3767–3804.

[8] Wang, W. N.; Gao, Y. C.; Jia, X. D.; Xi, K. A novel Au-Pt@PPy(polypyrrole) coral-like structure: Facile synthesis, high SERS effect, and good electro catalytic activity. *J. Colloid Interface Sci.* **2013**, *396*, 23–28.

[9] Yin, H. J.; Zhao, S. L.; Zhao, K.; Muqsit, A.; Tang, H. J.; Chang, L.; Zhao, H. J.; Gao, Y.; Tang, Z. Y. Ultrathin platinum nanowires grown on single-layered nickel hydroxide with high hydrogen evolution activity. *Nat. Commun.* **2015**, *6*, 6430.

[10] Kloke, A.; von Stetten, F.; Zengerle, R.; Kerzenmacher, S. Strategies for the fabrication of porous platinum electrodes. *Adv. Mater.* **2011**, *23*, 4976–5008.

[11] Li, C. L.; Sato, T.; Yamauchi, Y. Electrochemical synthesis of one-dimensional mesoporous Pt nanorods using the assembly of surfactant micelles in confined space. *Angew. Chem., Int. Ed.* **2013**, *52*, 8050–8053.

[12] Li, Z. Y.; Liang, Y. J.; Jiang, S. P.; Shan, X. D.; Lin, M. L.; Xu, C. W. Electrooxidation of methanol and ethylene glycol mixture on platinum and palladium in alkaline medium. *Fuel Cells* **2012**, *12*, 677–682.

[13] Qiu, Y.; Hu, Z.; Li, H.; Ren, Q.; Chen, Y.; Hu, S. Hybrid electrocatalyst Ag/Co/C via flash Joule heating for oxygen reduction reaction in alkaline media. *Chem. Eng. J.* **2022**, *430*, 132769.

[14] Furukawa, S.; Komatsu, T. Intermetallic compounds: Promising inorganic materials for well-structured and electronically modified reaction environments for efficient catalysis. *ACS Catal.* **2017**, *7*, 735–765.

[15] Xu, H.; Yan, B.; Zhang, K.; Wang, J.; Li, S. M.; Wang, C. Q.; Shiraishi, Y.; Du, Y. K.; Yang, P. Facile fabrication of novel PdRu nanoflowers as highly active catalysts for the electrooxidation of methanol. *J. Colloid Interface Sci.* **2017**, *505*, 1–8.

[16] Wang, Y.; Zheng, X. B.; Wang, D. S. Design concept for electrocatalysts. *Nano Res.* **2022**, *15*, 1730–1752.

[17] Wang, Y.; Zheng, M.; Li, Y. R.; Ye, C. L.; Chen, J.; Ye, J. Y.; Zhang, Q. H.; Li, J.; Zhou, Z. Y.; Fu, X. Z. et al. p–d Orbital hybridization induced by a monodispersed Ga site on a Pt_3Mn nanocatalyst boosts ethanol electrooxidation. *Angew. Chem., Int. Ed.* **2022**, *61*, e202115735.

[18] Qiu, Y. J.; Zhang, J.; Jin, J.; Sun, J. Q.; Tang, H. L.; Chen, Q. Q.; Zhang, Z. D.; Sun, W. M.; Meng, G.; Xu, Q. et al. Construction of Pd-Zn dual sites to enhance the performance for ethanol electro-oxidation reaction. *Nat. Commun.* **2021**, *12*, 5273.

[19] Xiao, W. P.; Lei, W.; Gong, M. X.; Xin, H. L.; Wang, D. Recent advances of structurally ordered intermetallic nanoparticles for electrocatalysis. *ACS Catal.* **2018**, *8*, 3237–3256.

[20] Espinosa, M. M. F.; Cheng, T.; Xu, M. J.; Abatemarco, L.; Choi, C.; Pan, X. Q.; Goddard III, W. A.; Zhao, Z. P.; Huang, Y. Compressed intermetallic PdCu for enhanced electrocatalysis. *ACS Energy Lett.* **2020**, *5*, 3672–3680.

[21] Kim, H. Y.; Kim, J. M.; Ha, Y.; Woo, J.; Byun, A.; Shin, T. J.; Park, K. H.; Jeong, H. Y.; Kim, H.; Kim, J. Y. et al. Activity origin and multifunctionality of Pt-based intermetallic nanostructures for efficient electrocatalysis. *ACS Catal.* **2019**, *9*, 11242–11254.

[22] Kumar, A.; Deka, S. PdSn hollow alloy nanoparticles prepared by *in-situ* galvanic replacement process for exclusive hydrogen evolution reaction and durable electrocatalysis. *Appl. Catal. A: General* **2020**, *599*, 117575.

[23] Shan, X. Y.; Sui, N.; Liu, W. G.; Liu, M. H.; Liu, J. *In situ* generation of supported palladium nanoparticles from a Pd/Sn/S chalcogel and applications in 4-nitrophenol reduction and Suzuki coupling. *J. Mater. Chem. A* **2019**, *7*, 4446–4450.

[24] Wu, Z. L.; Shih, Y. J. Bimetallic palladium-tin nanoclusters, PdSn (200) and PdSn (101), templated with cationic surfactant for electrochemical denitrification toward N_2 and NH^{4+} selectivity. *Chem. Eng. J.* **2022**, *433*, 133852.

[25] Freakley, S. J.; He, Q.; Harrhy, J. H.; Lu, L.; Crole, D. A.; Morgan, D. J.; Ntainjua, E. N.; Edwards, J. K.; Carley, A. F.; Borisevich, A. Y. et al. Palladium-tin catalysts for the direct synthesis of H_2O_2 with high selectivity. *Science* **2016**, *351*, 965–968.

[26] Xaba, N.; Modibedi, R. M.; Mathe, M. K.; Khotseng, L. E. Pd, PdSn, PdBi, and PdBiSn nanostructured thin films for the electro-oxidation of ethanol in alkaline media. *Electrocatalysis* **2019**, *10*, 332–341.

[27] Song, T. X.; Gao, F.; Zhang, Y. P.; Yu, P. E.; Wang, C.; Shiraishi, Y.; Li, S. J.; Wang, C. Q.; Guo, J.; Du, Y. K. Shape-controlled PdSn alloy as superior electrocatalysts for alcohol oxidation reactions. *J. Taiwan Inst. Chem. Eng.* **2019**, *101*, 167–176.

[28] Du, W. X.; Mackenzie, K. E.; Milano, D. F.; Deskins, N. A.; Su, D.; Teng, X. W. Palladium-tin alloyed catalysts for the ethanol oxidation reaction in an alkaline medium. *ACS Catal.* **2012**, *2*, 287–297.

[29] You, H. M.; Gao, F.; Wang, C.; Li, J.; Zhang, K. W.; Zhang, Y. P.; Du, Y. K. Rich grain boundaries endow networked PdSn nanowires with superior catalytic properties for alcohol oxidation. *Nanoscale* **2021**, *13*, 17939–17944.

[30] Zhang, Y.; Huang, B. L.; Shao, Q.; Feng, Y. G.; Xiong, L. K.; Peng, Y.; Huang, X. Q. Defect engineering of palladium-tin nanowires enables efficient electrocatalysts for fuel cell reactions. *Nano Lett.* **2019**, *19*, 6894–6903.

[31] Chen, Q. L.; Yang, Y. N.; Cao, Z. M.; Kuang, Q.; Du, G. F.; Jiang, Y. Q.; Xie, Z. X.; Zheng, L. S. Excavated cubic platinum-tin alloy nanocrystals constructed from ultrathin nanosheets with enhanced electrocatalytic activity. *Angew. Chem., Int. Ed.* **2016**, *55*, 9021–9025.

[32] Yin, Y. D.; Rioux, R. M.; Erdonmez, C. K.; Hughes, S.; Somorjai, G. A.; Alivisatos, A. P. Formation of hollow nanocrystals through the nanoscale kirkendall effect. *Science* **2004**, *304*, 711–714.

[33] Shapiro, A.; Jang, Y.; Horani, F.; Kauffmann, Y.; Lifshitz, E. Kirkendall effect: Main growth mechanism for a new SnTe/PbTe/SnO_2 nano-heterostructure. *Chem. Mater.* **2018**, *30*, 3141–3149.

[34] Anderson, B. D.; Tracy, J. B. Nanoparticle conversion chemistry: Kirkendall effect, galvanic exchange, and anion exchange. *Nanoscale* **2014**, *6*, 12195–12216.

[35] Guo, X. Y.; Hu, Z.; Lv, J. X.; Li, H.; Zhang, Q. H.; Gu, L.; Zhou, W.; Zhang, J. W.; Hu, S. Fine-tuning of Pd-Rh core–shell catalysts by interstitial hydrogen doping for enhanced methanol oxidation. *Nano Res.* **2022**, *15*, 1288–1294.